

Million-Q integrated Fabry-Perot cavity using ultralow-loss multimode retroreflectors

HONGNAN XU,  YUE QIN, GAOLEI HU, AND HON KI TSANG* 

Department of Electronic Engineering, The Chinese University of Hong Kong, Shatin, New Territories, Hong Kong, China

*Corresponding author: hksang@ee.cuhk.edu.hk

Received 15 July 2022; revised 15 August 2022; accepted 31 August 2022; posted 1 September 2022 (Doc. ID 470644); published 24 October 2022

The monolithic integration of Fabry-Perot cavities has many applications, such as label-free sensing, high-finesse filters, semiconductor lasers, and frequency comb generation. However, the excess loss of integrated reflectors makes it challenging to realize integrated Fabry-Perot cavities working in the ultrahigh- Q regime ($>10^6$). Here, we propose and experimentally demonstrate what we believe is the first silicon integrated million- Q Fabry-Perot cavity. Inspired by free-space optics, a novel monolithically integrated retroreflector is utilized to obtain near-unity reflectance and negligible reflection losses. The corner scattering in the retroreflector is prevented by the use of the TE_1 mode, taking advantage of its zero central field intensity. Losses incurred by other mechanisms are also meticulously engineered. The measurement results show resonances with an ultrahigh intrinsic Q factor of $\approx 3.4 \times 10^6$ spanning an 80-nm bandwidth. The measured loaded Q factor is $\approx 2.1 \times 10^6$. Ultralow reflection losses (≈ 0.05 dB) and propagation losses (≈ 0.18 dB/cm) are experimentally realized. © 2022 Chinese Laser Press

<https://doi.org/10.1364/PRJ.470644>

1. INTRODUCTION

Fabry-Perot (FP) cavities confine light between a pair of reflectors in the form of a standing wave [1]. Due to its sharp spectral responses and capability for field enhancement, the FP cavity plays a central role in a vast range of applications, e.g., wavemeters [2], gravity-wave detection [3], label-free sensing [4], semiconductor lasers [5], linewidth narrowing [6], quantum-information processing [7], frequency comb generation [8,9], and high-capacity communications [10,11]. Compared to traveling-wave cavities, FP cavities have some unique applications due to the standing-wave property, such as cavity-enhanced optical trapping [12] and atom cooling [13]. In addition, bent waveguides are not required in FP cavities, leading to a smaller footprint and a higher integration density. Silicon-on-insulator (SOI) has become a mainstream platform for photonic integration, thanks to its scalability, high yield, and CMOS compatibility [14]. A variety of FP cavities on SOI have been investigated in recent research [8–11,15–22], but their Q factors are all quite limited. The photonic-crystal (PhC) nanocavity can offer high Q factors by trapping the resonant mode in a photonic bandgap [23]. However, the nanocavity mode in PhCs cannot be depicted by FP mechanisms when the cavity length only involves few PhC lattices [24]. Longer FP cavities formed by PhC waveguides have been experimentally characterized, but their Q factors cannot exceed one million [24,25]. To date, the ultrahigh- Q ($>10^6$) silicon-integrated FP cavity has not yet been demonstrated.

Unlike traveling-wave cavities, such as microring resonators [26,27] and microdisk resonators [28,29], whose intrinsic Q factors are predominantly governed by propagation loss, FP cavities also suffer from excess losses of reflectors. In order to improve the Q factor of FP cavities, it is essential to reduce the reflection loss. The distributed Bragg reflector (DBR) is the most commonly used on-chip reflector. The DBR relies on grating structures to form the constructive interference of multiple reflected waves. Typically, DBRs can be realized by introducing sidewall corrugations [8–10,16–18], embedded nanoholes [15], and deep trenches [19,20,30]. However, the requirement for broadband reflection necessitates the use of high-contrast gratings with strong out-of-plane diffraction losses [31]. For a silicon-integrated DBR, such diffraction losses can be as high as 5% [19,30] unless the trench depth is scaled up to several micrometers [20]. Therefore, the Q factor of most DBR-based FP cavities is restricted to the order of 10^4 [10,19,20]. In Refs. [8,9], silicon-nitride-on-insulator (SNOI) with a lower index contrast is exploited to alleviate diffraction losses and lift the Q factor to $\approx 4.8 \times 10^5$ in a narrow bandwidth, but a higher Q factor ($>10^6$) has remained unattainable. As an alternative, on-chip reflectors can also be built by connecting the output ports of a 3-dB coupler to a looped waveguide [11]. The performance of loop structures is, however, limited by the scattering loss in Y-junctions [32] or multimode interference couplers [33]. The scattering loss can be inhibited by using directional couplers (DCs) [34]. Nevertheless, the coupling ratio of DCs is

usually susceptible to fabrication defects and typically has a limited optical bandwidth, making it difficult to attain near-unity reflectance over a broad bandwidth. The reported Q factor of loop-based FP cavities is limited to $\approx 2.3 \times 10^4$ [11]. Other types of on-chip reflectors, such as coated metallic mirrors [21] and inverse-designed structures [22], all suffer from the intrinsically high reflection loss caused by ohmic absorption or stringent feature sizes; hence, the measured Q factors cannot exceed $\approx 2.0 \times 10^3$. The ultralow-loss on-chip reflector for ultrahigh- Q ($> 10^6$) FP cavities has remained an unsolved open problem.

In this work, we present the first demonstration on million- Q silicon-integrated FP cavities. Inspired by free-space optics, a nearly lossless retroreflector is developed to address the reflection loss issue. By employing the TE_1 mode with zero central field intensity, the scattering loss is minimized at the corner region of retroreflectors. Losses from other mechanisms are also reduced to an ultralow level. An ultrahigh intrinsic Q factor ($\approx 3.4 \times 10^6$) is experimentally achieved. The maximum loaded Q factor is measured to be $\approx 2.1 \times 10^6$.

2. DESIGN AND ANALYSIS

Figures 1(a) and 1(b) depict the schematic configuration of the proposed FP cavity, which consists of an asymmetric directional

coupler (ADC) in the middle, a pair of reflectors at each end, and adiabatically tapered waveguides as connectors. The cavity is fed by an accessing waveguide through weak side coupling with a $\pi/2$ phase shift in the ADC. The tapered waveguide introduces a round-trip group delay, thereby building up a standing-wave resonance in the cavity. The dropped carrier experiences another $\pi/2$ phase shift, resulting in the total π phase shift. At the output port, the destructive interference will dramatically diminish the field intensity for resonant wavelengths, leading to the all-pass filtering of light [21,22]. The on-resonance carriers are reflected back into the input port.

In such a design, loss mechanisms can be categorized into four classes: the propagation loss produced by sidewall roughness, the intermodal conversion in tapered waveguides, the coupling loss in the ADC, and the reflection loss at reflectors, as illustrated in Fig. 1(c). As previously stated, the primary concern is to reduce the reflection loss. Here, we introduce the on-chip retroreflector to realize ultralow-loss reflection, as illustrated in Fig. 1(d). The structure is formed by two total-internal-reflection (TIR) mirrors at an angle of 90° . In a wide waveguide, the guided mode can be approximated as a cluster of weakly divergent rays [35]. Through the TIR effect, each ray will consecutively bounce off at A and A' [36]. Moreover, outer rays strike the mirror earlier than interior rays yet travel a longer

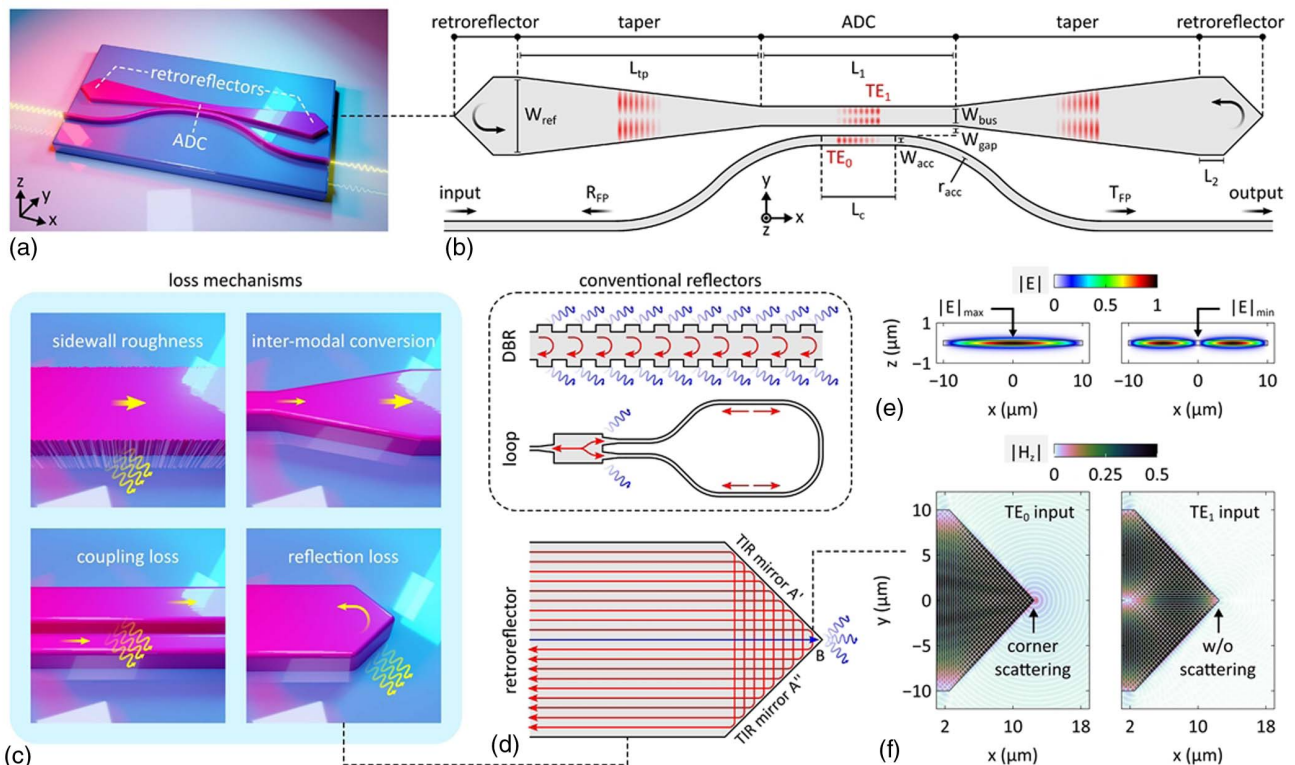


Fig. 1. Conceptual illustration of the FP cavity. (a) 3D view of the FP cavity; (b) schematic configuration of the FP cavity with key parameters labeled. The side coupling is accomplished by using an ADC. The cavity is terminated by a pair of retroreflectors at each end. (c) Illustration of loss mechanisms in the FP cavity; (d) working principle of the retroreflector. Other types of reflectors are also illustrated for comparison. The guided mode in a wide waveguide can be modeled by treating it as a cluster of rays. Each ray will bounce off at mirrors A and A' via TIR. The corner scattering at the point B contributes the greatest to reflection losses. (e) Calculated electric field profiles of TE_0 and TE_1 modes; for TE_1 , the field intensity is zero at the central position, thereby depressing the corner scattering completely. (f) Calculated light propagation profiles for the retroreflector when TE_0 and TE_1 modes are launched. The image contrast is enhanced to clearly show the scattering wave. The scattering loss is significantly mitigated when the TE_1 mode is injected.

transverse distance, resulting in identical light-path lengths for all launched rays. Thus, the input mode can be reflected while preserving its initial phase profile perfectly. The archetype of this structure, well known as the roof prism [37], has served as a fundamental element in numerous free-space optical systems. The retroreflection mechanism is ineffective at the corner point B , where mirrors A and A' are joined together, as illustrated in Fig. 1(d). Such corner scattering is the prime cause of reflection losses for on-chip retroreflectors. The TE_1 mode is employed to tackle this issue. The maximum field intensity of the TE_0 mode occurs at the central position, as shown in the left panel of Fig. 1(e). In contrast, the central field intensity of the TE_1 mode is zero, as shown in the right panel of Fig. 1(e). Consequently, the corner scattering can be naturally prevented by choosing the TE_1 mode to carry resonances. Figure 1(f) shows the calculated light propagation profiles when TE_0 and TE_1 modes are injected. For TE_1 , the corner scattering is significantly mitigated, since all the launched rays reside only on two lateral sides. In the following sections, we will analyze and optimize all the essential components in the proposed FP cavity to achieve an ultrahigh Q factor.

The design is implemented on the SOI platform consisting of a silicon core with $H_{wg} = 220$ nm and a silicon-dioxide buffer with $H_{buff} = 3$ μm . The upper cladding is a silicon-dioxide layer with a thickness of $H_{clad} = 1$ μm . The central wavelength is chosen as $\lambda = 1.55$ μm . The reference data for refractive indices can be found in Ref. [38]. We calculate the TE_1 effective index ($n_{eff,TE1}$) with varying widths (W_{wg}) by using the finite-difference frequency-domain (FDFD) method [39], as shown in Fig. 2(a). It can be observed that $n_{eff,TE1}$

converges to the effective index of the slab mode ($n_{slab} \approx 2.845$) when W_{wg} is large enough. Under the ray-optic approximation, the TIR angle (θ_{TIR}) can be obtained by using the equation below,

$$\theta_{TIR} = \arcsin \frac{n_{SiO_2}}{n_{slab}}, \quad (1)$$

where n_{SiO_2} denotes the refractive index of silicon dioxide. Figure 2(b) shows the calculated dispersion curve of θ_{TIR} . It can be found that θ_{TIR} is almost invariant over a 100-nm wavelength range. Thus, the TIR condition (i.e., $\theta_{TIR} < 45^\circ$) can be fulfilled for mirrors A and A' regardless of working wavelengths.

The reflectance is then calculated for the retroreflector as its width (W_{ref}) is varied, as shown in Fig. 2(c). The simulation is carried out by using the finite-difference time-domain (FDTD) method [39]. For comparison, both TE_0 and TE_1 are considered in the simulation. The TE_0 and TE_1 reflectance ($R_{ref,TE0}$, $R_{ref,TE1}$) are extracted by applying mode decomposition on the reflected wave [39]. For TE_0 and TE_1 , the calculated reflectance rises as W_{ref} increases, suggesting that the lateral divergence of light is mitigated, and the ray-optic approximation is valid. However, for TE_0 , the maximum reflectance can only reach $R_{ref,TE0} \approx 0.946$ due to the strong corner scattering. In contrast, for TE_1 , the near-unity reflectance ($R_{ref,TE1} \approx 0.993$) can be attained when the width is optimized to be $W_{ref} = 20$ μm . Here, the large modal area is also advantageous for the reduction of propagation losses, since the field intensity is diminished at sidewalls [40]. For a narrower width, e.g., $W_{ref} = 7.5$ μm , the reflectance is still quite high

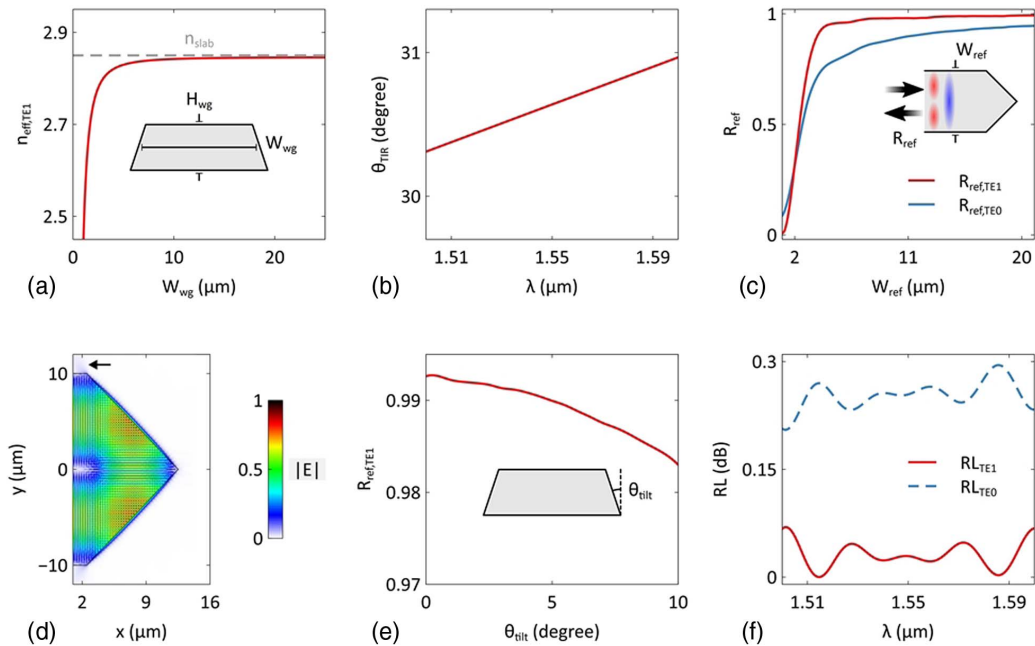


Fig. 2. Analysis and optimization of the retroreflector. (a) Calculated TE_1 effective indices ($n_{eff,TE1}$) with varying waveguide widths (W_{wg}). The dashed line represents the effective index of the slab mode (n_{slab}). The inset shows the waveguide cross section. (b) Calculated TIR angles (θ_{TIR}) with varying wavelengths; (c) calculated reflectance ($R_{ref,TE0}$, $R_{ref,TE1}$) with varying retroreflector widths (W_{ref}). The inset shows the structural top view. The near-unity reflectance can be achieved for TE_1 . (d) Calculated light propagation profile for the optimized retroreflector. The arrow shows the side-scattering effect. (e) Calculated $R_{ref,TE1}$ with varying sidewall tilt angles (θ_{tilt}). The inset shows the waveguide cross section. (f) Calculated TE_1 -reflection-loss (RL_{TE1}) spectrum for the optimized retroreflector. The dashed line shows the calculated TE_0 reflection losses (RL_{TE0}).

($R_{\text{ref,TE1}} \approx 0.975$), making the proposed reflector well suited for optical filters with smaller footprints and relatively lower Q factors. Figure 2(d) shows the calculated light propagation profile with $W_{\text{ref}} = 20 \mu\text{m}$. From the profile, high reflectance and negligible corner scattering can be observed. A slanted waveguide sidewall may arise because of the difficulty in the precise control of dry-etching processes. The inclination of sidewalls in retroreflectors will introduce excess losses [41]. To address this concern, we also calculate the reflectance as a function of the sidewall tilt angle (θ_{tilt}), as shown in Fig. 2(e). High reflectance of $R_{\text{ref,TE1}} > 0.99$ can still be accomplished, even with a considerably large sidewall tilt angle, e.g., $\theta_{\text{tilt}} = 5^\circ$. Such perpendicularity can be ensured by most silicon photonic foundries. The reflection loss ($\text{RL}_{\text{TE}i} = -10 \log_{10} R_{\text{ref,TE}i}$) is then calculated to further evaluate the performance, as shown in Fig. 2(f). The calculation results show ultralow reflection losses of $\text{RL}_{\text{TE1}} \approx 0.01\text{--}0.07 \text{ dB}$ for TE_1 over a 100-nm bandwidth. Around the central wavelength, the reflection loss is reduced by $>0.2 \text{ dB}$ compared to the TE_0 case. In addition, RL is also slightly affected by the side scattering [see the arrow in

Fig. 2(d)], and its strength is tied to the (anti-)node position of lateral standing waves. The ripples in RL spectra are opposite between TE_0 and TE_1 , since their symmetries are inverted and the positions of nodes and antinodes are exchanged.

The ADC is leveraged to achieve the side coupling between TE_0 and TE_1 . The cross-talk-free TE_0 -to- TE_1 conversion relies on the perfect matching between $n_{\text{eff,TE0}}$ of the accessing waveguide and $n_{\text{eff,TE1}}$ of the bus waveguide [42]. Figure 3(a) shows the calculated $n_{\text{eff,TE0}}$ and $n_{\text{eff,TE1}}$ with varying widths. The combination of accessing-waveguide and bus-waveguide widths (W_{acc} , W_{bus}) can be then determined according to the phase-matching condition. The coupling loss is calculated for the ADC with various structural parameters, as shown in Figs. 3(b) and 3(c). Here, the coupling loss is defined as $\text{CL} = 10 \log_{10}(T_{\text{BAR}} + T_{\text{CRO,TE1}})$, where T_{BAR} denotes the remnant transmittance in the accessing waveguide, and $T_{\text{CRO,TE1}}$ denotes the TE_1 coupling ratio. In the simulation, the gap width is set as $W_{\text{gap}} = 300 \text{ nm}$ to ensure a large feature size and easy gap filling. The coupling loss in an ADC is usually sensitive to the perturbation caused by strong evanescent

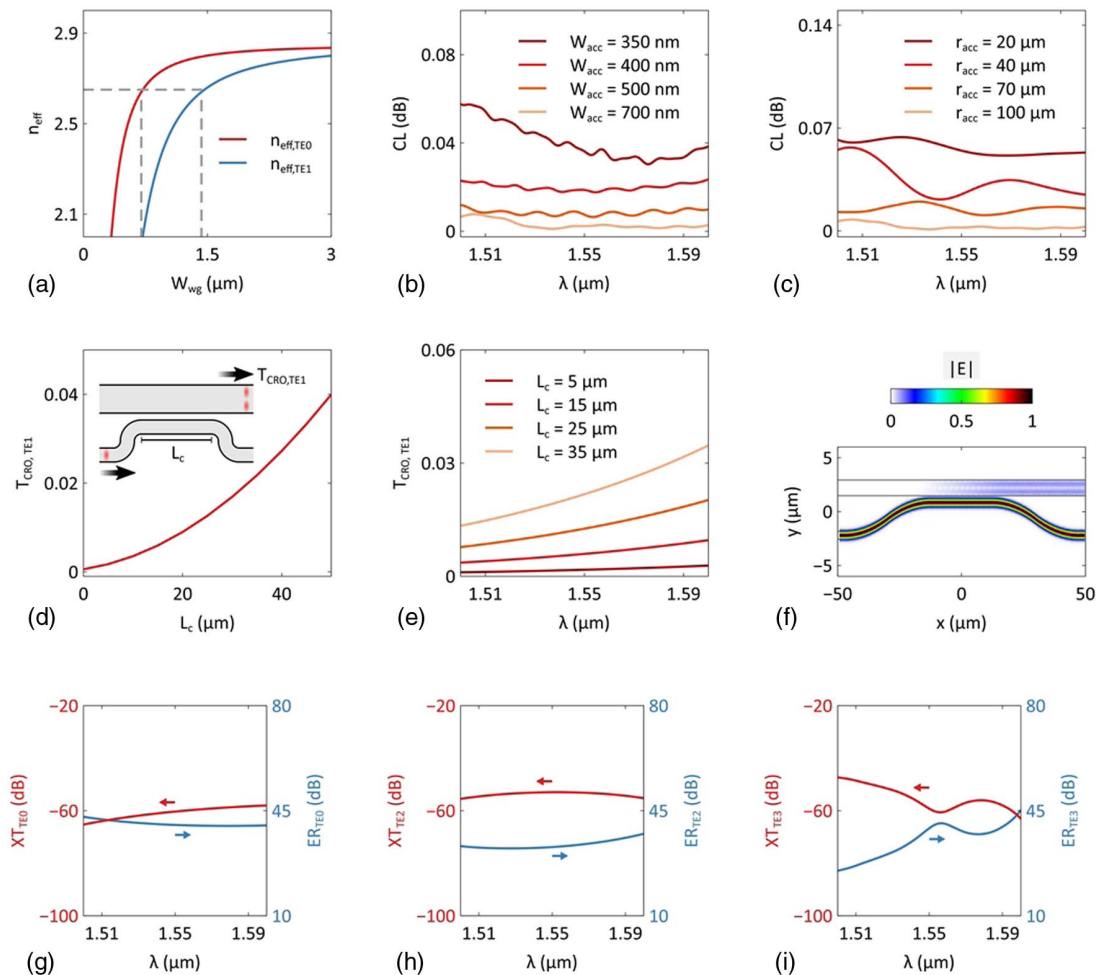


Fig. 3. Analysis and optimization of the ADC. (a) Calculated TE_0 and TE_1 effective indices ($n_{\text{eff,TE0}}$, $n_{\text{eff,TE1}}$) with varying waveguide widths (W_{wg}); the dashed lines show the phase matching between TE_0 and TE_1 modes. Calculated coupling-loss (CL) spectra with different (b) widths (W_{acc}) and (c) bending radii (r_{acc}) of the accessing waveguide; (d) calculated TE_1 coupling ratio ($T_{\text{CRO,TE1}}$) with varying coupling lengths (L_c). The inset shows the structural top view. (e) Calculated $T_{\text{CRO,TE1}}$ spectra with different L_c ; (f) calculated light propagation profile for the optimized ADC; (g)–(i) calculated intermodal cross talk (XT_{TE0} , XT_{TE2} , XT_{TE3}) and extinction-ratio (ER_{TE0} , ER_{TE2} , ER_{TE3}) spectra for the optimized ADC.

coupling, since the transmission of higher-order modes is more vulnerable. Therefore, we tend to choose a wide width ($W_{\text{acc}} = 700 \text{ nm}$) to depress the evanescent field intensity and a large bending radius ($r_{\text{acc}} = 100 \mu\text{m}$) to ensure the gradual approaching of accessing and bus waveguides, thereby establishing an adiabatic coupling process [26]. According to Fig. 3(a), the bus-waveguide width is then determined as $W_{\text{bus}} = 1.428 \mu\text{m}$. The optimal coupling loss is as low as $\text{CL} < 0.01 \text{ dB}$ over a 100-nm wavelength range. Figure 3(d) shows the calculated $T_{\text{CRO,TE}_1}$ with varying coupling lengths (L_c). Figure 3(e) shows the corresponding $T_{\text{CRO,TE}_1}$ spectra. To enable high- Q resonances, the coupling length is chosen as $L_c = 25 \mu\text{m}$, with a weak coupling ratio of $T_{\text{CRO,TE}_1} \approx 0.01$. Figure 3(f) shows the calculated light propagation profile for the optimized ADC. An efficient TE_0 -to- TE_1 conversion and a weak coupling strength can be clearly observed. In total, four TE modes (i.e., TE_{0-3}) are supported by the bus

waveguide with $W_{\text{bus}} = 1.428 \mu\text{m}$. To verify the mode selectivity, intermodal cross talks ($\text{XT}_{\text{TE}_i} = 10 \log_{10} T_{\text{CRO,TE}_i}$) and extinction ratios ($\text{ER}_{\text{TE}_i} = 10 \log_{10} T_{\text{CRO,TE}_1} / T_{\text{CRO,TE}_i}$) are calculated for the optimized ADC [see Figs. 3(g)–3(i)]. Around the central wavelength, low cross talks ($\text{XT}_{\text{TE}_i} < -50 \text{ dB}$) and high extinction ratios ($\text{ER}_{\text{TE}_i} > 30 \text{ dB}$) can be attained, so that only resonances carried by the TE_1 mode will be excited in the FP cavity. In addition, high performance can be maintained despite fabrication defects, as detailed in Appendix A.

The propagation loss is mainly induced by the sidewall roughness. The volume-current method is used to model this stochastic process by making sidewall nonuniformity as polarized current sources equivalent. The detailed description of this method can be found in Ref. [43]. In Fig. 4(a), we present the calculated propagation losses (α_{TE_1}) with varying W_{wg} under different mean deviations of roughness (σ). Here, the

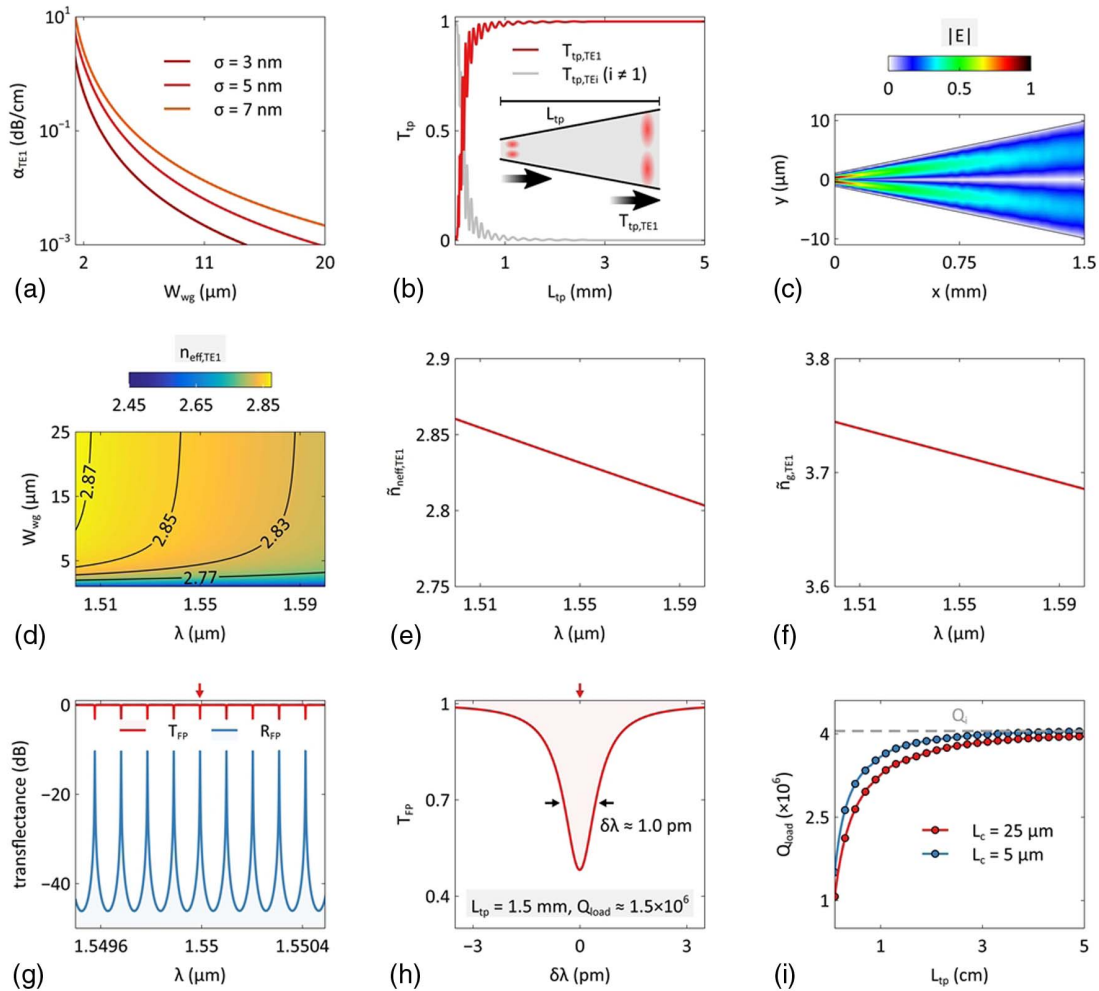


Fig. 4. Analysis and optimization of the FP cavity. (a) Calculated TE_1 propagation losses (α_{TE_1}) with varying waveguide widths (W_{wg}) under different mean deviations of sidewall roughness (σ); (b) calculated transmission efficiencies ($T_{\text{tp,TE}_i}$) with varying taper lengths (L_{tp}); the inset shows the structural top view. (c) Calculated light propagation profile for the tapered waveguide with $L_{\text{tp}} = 1.5 \text{ mm}$; (d) calculated TE_1 effective indices ($n_{\text{eff,TE}_1}$) as a two-dimensional map in terms of W_{wg} and wavelengths; calculated (e) mean effective indices ($\bar{n}_{\text{eff,TE}_1}$) and (f) mean group indices (\bar{n}_{g,TE_1}) of the TE_1 mode with varying wavelengths; (g) calculated transmittance (T_{FP}) and reflectance (R_{FP}) spectra for the FP cavity with $L_{\text{tp}} = 1.5 \text{ mm}$; (h) zoom-in view of the T_{FP} spectrum in the vicinity of a single resonance. The red arrow indicates the corresponding spectral position in (g). (i) Calculated loaded Q factors (Q_{load}) with varying L_{tp} ; the dashed line represents the intrinsic Q factor (Q_i). An ultrahigh intrinsic Q factor of $Q_i \approx 4.1 \times 10^6$ is attained.

correlation length of roughness is assumed to be 50 nm [43]. The propagation loss can be reduced to an extremely low level ($\alpha_{\text{TE1}} < 0.01$ dB/cm) when the waveguide is quite wide (e.g., $W_{\text{wg}} > 10$ μm). In the tapered waveguide, the taper width varies linearly from W_{bus} to W_{ref} ; hence, the taper length (L_{tp}) must be carefully designed to avoid the intermodal conversion. Figure 4(b) shows the calculated TE_1 transmission efficiencies ($T_{\text{tp,TE1}}$) with varying L_{tp} by using the eigenmode expansion (EME) method. The conversion from TE_1 to other modes can be fully eliminated (i.e., $T_{\text{tp,TE1}} \approx 1$) when the taper length is long enough ($L_{\text{tp}} > 1$ mm). The calculated light propagation profile for the tapered waveguide with $L_{\text{tp}} = 1.5$ mm is shown in Fig. 4(c). Other types of taper trajectories can also be adopted to define the waveguide shape and reduce the device footprint [44]. In this work, it is unnecessary to further shorten the taper length, since the long round-trip length is a desirable attribute in the realization of ultrahigh Q factors. In a slow-varying taper, light transmission can be described by the following equations [45]:

$$E = E_0 \sqrt{T_{\text{tp,TE1}}} 10^{-\tilde{\alpha}_{\text{TE1}} L_{\text{tp}}/20} e^{ik_0 \tilde{n}_{\text{eff,TE1}} L_{\text{tp}}}, \quad (2)$$

$$\tilde{n}_{\text{eff,TE1}} = \int_{L=0}^{L_{\text{tp}}} n_{\text{eff,TE1}} dL/L_{\text{tp}}, \quad (3)$$

$$\tilde{\alpha}_{\text{TE1}} = \int_{L=0}^{L_{\text{tp}}} \alpha_{\text{tp}} dL/L_{\text{tp}}, \quad (4)$$

where E_0 and E denote the magnitudes of electric field at the beginning and end of the tapered waveguide, k_0 denotes the vacuum wavenumber, $\tilde{n}_{\text{eff,TE1}}$ denotes the mean effective index, and $\tilde{\alpha}_{\text{TE1}}$ denotes the mean propagation loss. Figure 4(d) shows the calculated $n_{\text{eff,TE1}}$ map in terms of W_{wg} and wavelengths. The $\tilde{n}_{\text{eff,TE1}}$ spectrum can be then obtained according to Eq. (3), as shown in Fig. 4(e). In addition, we also calculate the corresponding mean group indices ($\tilde{n}_{g,\text{TE1}} = \tilde{n}_{\text{eff,TE1}} - \lambda \cdot \partial \tilde{n}_{\text{eff,TE1}} / \partial \lambda$), as shown in Fig. 4(f). By using Eq. (4), the mean propagation loss is calculated to be $\tilde{\alpha}_{\text{TE1}} \approx 0.15$ dB/cm with $\sigma = 5$ nm at the central wavelength of 1.55 μm . Further calculations show that $\tilde{\alpha}_{\text{TE1}}$ is nearly wavelength-independent, which is due to the large modal area. Both $\tilde{n}_{\text{eff,TE1}}$ and $\tilde{\alpha}_{\text{TE1}}$ are independent with L_{tp} because of the linear taper trajectory. By using Eqs. (3) and (4), the tapered waveguide can be substituted by an equivalent straight waveguide to simplify the modeling of FP cavities.

Eventually, all the essential components in the FP cavity have been optimized. The optimal structural parameters are listed as follows: $W_{\text{ref}} = 20$ μm , $W_{\text{acc}} = 700$ nm, $W_{\text{bus}} = 1.428$ μm , $W_{\text{gap}} = 300$ nm, $L_c = 25$ μm , $L_{\text{tp}} > 1$ mm, $L_1 = 50$ μm , and $L_2 = 10$ μm . Here, L_1 and L_2 refer to the lengths of straight sections in between retroreflectors and tapers. By using the transient sample mode time-domain (TSM TD) method [39], the transmittance (T_{FP}) and reflectance (R_{FP}) spectra are obtained for the optimized FP cavity. Here, each component is described by a transfer matrix, which is readily available in Lumerical cosimulation suites [39]. In the simulation, the sidewall roughness is set as $\sigma = 5$ nm, as an example. Figure 4(g) shows the calculated T_{FP} and R_{FP} spectra for the FP cavity with $L_{\text{tp}} = 1.5$ mm. At resonant wavelengths,

the summation of T_{FP} and R_{FP} is nonunity, since a portion of energy is dissipated by intracavity losses. Figure 4(h) is the zoom-in view of the T_{FP} spectrum in the vicinity of a single resonance. The 3-dB bandwidth is calculated to be $\delta\lambda \approx 1.0$ pm with the corresponding loaded Q factor of $Q_{\text{load}} \approx 1.5 \times 10^6$. A high extinction ratio of $\text{ER}_{\text{res}} \approx 3.2$ dB can be attained at the resonant wavelength. The calculated Q_{load} rises as L_{tp} increases [see Fig. 4(i)], since the adiabatic taper constitutes the majority of the round-trip length. To determine the intrinsic Q factor, we also calculate the $L_{\text{tp}} - Q_{\text{load}}$ curve with a reduced coupling length ($L_c = 5$ μm) and a near-zero coupling ratio ($T_{\text{CRO,TE1}} \approx 0.001$). The intrinsic quality factor is estimated to be $Q_i \approx 4.1 \times 10^6$ when the taper length is extended to $L_{\text{tp}} > 5$ cm.

3. FABRICATION AND CHARACTERIZATION

An array of FP cavities with varying L_{tp} was fabricated at Applied Nanotools Inc. [46] by applying electron beam lithography (EBL) and reactive ion etching (RIE) on a commercial SOI wafer, as shown in Figs. 5(a) and 5(b). An oxide upper cladding was deposited through plasma-enhanced chemical vapor deposition (PECVD). Titanium–tungsten heaters were patterned on the top of FP cavities to offer thermo-optical tunability. Efficient edge coupling with lensed fibers is enabled by leveraging inverse tapers [47]. On-chip polarizers were monolithically integrated with inverse tapers to ensure single-polarization operations [48]. Several straight waveguides were fabricated in close proximity for normalization purposes.

Figure 5(c) illustrates the measurement setup. The fabricated devices were characterized by scanning the wavelength of a narrow-linewidth tunable laser (Keysight 8164B) while reading the output power from a synchronized high-detectivity power meter (Keysight 81636B). The polarization state was adjusted by a polarization controller (PC). The chip was mounted on a thermo-electric cooler (TEC) to stabilize the ambient temperature. We used an optical isolator to filter out the reflected light, since the performance of an FP cavity can be fully depicted by its T_{FP} spectrum. Figure 5(d) shows the measured T_{FP} spectra around $\lambda \approx 1.55$ μm with varying L_{tp} . In Figs. 5(e) and 5(f), we show the T_{FP} spectra in the vicinity of a single resonance with $L_{\text{tp}} = 1.5$ mm and 4.0 mm. By applying Lorentz fitting, loaded Q factors are characterized to be $Q_{\text{load}} \approx 1.1 \times 10^6$ and 1.9×10^6 , respectively. The measured line shape is virtually symmetric even if the launched laser power is up to -5 dBm, indicating a cold-cavity state and suppressed optothermal responses. This phenomenon originates in the large modal area of multimode waveguides. Numerous applications can benefit from the optothermal stability, such as linewidth narrowing [6] and frequency stabilization [49]. The measured $L_{\text{tp}} - Q_{\text{load}}$ curve is shown in Fig. 5(g). Here, the measurement error is estimated by the standard deviation of Q_{load} obtained from several neighboring resonances. In Appendix B, we also measured the T_{FP} spectra at different wavelength bands. Due to the dispersion of $T_{\text{CRO,TE1}}$, the measured Q_{load} is higher at shorter wavelengths. In the experiment, we observe a maximum loaded Q factor of $Q_{\text{load}} \approx 2.1 \times 10^6$ around $\lambda \approx 1.51$ μm . It is impossible to obtain the intrinsic Q factor by directly measuring the 3-dB bandwidth of resonances,

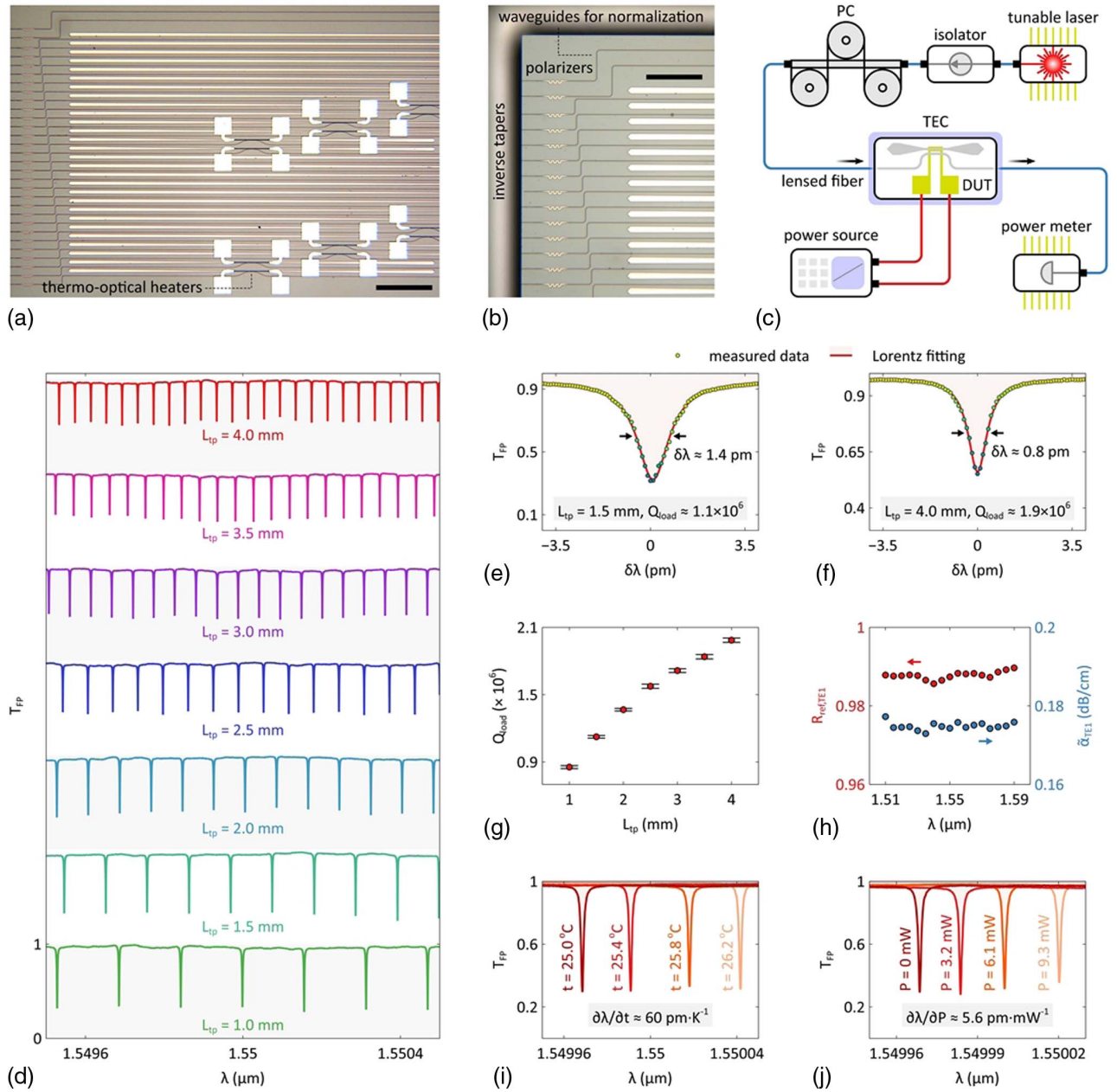


Fig. 5. Experimental results for the fabricated FP cavities. (a), (b) Microscopic images of the fabricated devices; the scale bars represent 350 and 200 μm , respectively. (c) Schematic configuration of the measurement setup; (d) measured transmittance (T_{FP}) spectra with varying taper lengths (L_{tp}). For clarity, a progressive shift is applied on the plotted spectra. Zoom-in views of the T_{FP} spectra in the vicinity of a single resonance with (e) $L_{\text{tp}} = 1.5$ mm and (f) 4.0 mm; (g) measured loaded Q factors (Q_{load}) with varying L_{tp} ; (h) reconstructed reflectance ($R_{\text{ref,TE1}}$) and mean-propagation-loss ($\tilde{\alpha}_{\text{TE1}}$) spectra; (i) measured T_{FP} spectra at different ambient temperatures (t); (j) measured thermo-optical responses with varying electric power (P) applied. PC, polarization controller; TEC, thermo-electric cooler; DUT, device under test.

since the cavity length is constrained by the die size. Here, we propose to use the cavity-scattering theorem to resolve Q_i [21]. To achieve this, it is necessary to extract several hidden parameters (i.e., $R_{\text{ref,TE1}}$, $\tilde{\alpha}_{\text{TE1}}$, and $T_{\text{CRO,TE1}}$) from the measured T_{FP} spectra by using the following equations:

$$Q_{\text{load}} = \frac{k_0 L_{\text{FP}} \tilde{n}_{g,\text{TE1}}}{(R_{\text{ref,TE1}} a)^{-1} + T_{\text{CRO,TE1}} - 1}, \quad (5)$$

$$\text{ER}_{\text{res}} = 10 \log_{10} \left[\frac{1 + R_{\text{ref,TE1}} a}{1 - R_{\text{ref,TE1}} a} \cdot \frac{1 - R_{\text{ref,TE1}} a (1 - T_{\text{CRO,TE1}})}{1 + R_{\text{ref,TE1}} a (1 - T_{\text{CRO,TE1}})} \right]^2, \quad (6)$$

$$\text{FSR} = \frac{\lambda^2}{2L_{\text{FP}} \tilde{n}_{g,\text{TE1}}}, \quad (7)$$

where FSR denotes the free spectral range, L_{FP} denotes the cavity length ($\approx L_1 + 2L_2 + 2L_{\text{tp}}$), $\tilde{n}_{g,\text{TE1}}$ denotes the mean group

index throughout the cavity, and a denotes the attenuation over L_{FP} . Three unknown variants (i.e., $L_{\text{FP}} - \tilde{n}_{g,\text{TE}_1}$ product, $R_{\text{ref,TE}_1} - a$ product, and $T_{\text{CRO,TE}_1}$) can be derived from Eqs. (5)–(7) given the measured Q_{load} , ER_{res} , and FSR (see Appendix B). The propagation loss dominates the attenuation process; hence, the $R_{\text{ref,TE}_1} - a$ product can be formulated as a log-scale linear regression on L_{FP} ,

$$10 \log_{10} R_{\text{ref,TE}_1} a = -\tilde{\alpha}_{\text{TE}_1} L_{\text{FP}} / 10 + 10 \log_{10} R_{\text{ref,TE}_1}. \quad (8)$$

From Eq. (8), $R_{\text{ref,TE}_1}$ and $\tilde{\alpha}_{\text{TE}_1}$ can be reconstructed by using the intercept and slope of the regression curve. This method is applied at different wavelengths; the reconstruction results are shown in Fig. 5(h). The reflectance is measured to be $R_{\text{ref,TE}_1} \approx 0.99$, with a flattened dispersion over an 80-nm bandwidth. The corresponding reflection loss is $RL_{\text{TE}_1} \approx 0.05$ dB, which is in good agreement with the simulation results. The measured propagation loss is $\tilde{\alpha}_{\text{TE}_1} \approx 0.18$ dB/cm. This loss level is quite close to the experimental results demonstrated in Ref. [50]. The reconstructed $T_{\text{CRO,TE}_1}$ spectrum is presented in Appendix B. The intrinsic Q factor is then estimated to be $Q_i \approx 3.4 \times 10^6$ by assuming $T_{\text{CRO,TE}_1} \rightarrow 0$ and $L_{\text{FP}} \rightarrow \infty$ in Eq. (5). Figure 5(i) shows the measured T_{FP} spectra at different ambient temperatures (t). The temperature sensitivity is measured to be $\partial\lambda/\partial t \approx 60$ pm/K. The thermo-optical tuning was implemented by applying different electric power (P) with a power source (Keithley 2400), as shown in Fig. 5(j). A high tuning efficiency of $\partial\lambda/\partial P \approx 5.6$ pm/mW is experimentally realized.

4. CONCLUSION AND DISCUSSION

In this work, we report a silicon-integrated FP cavity with an ultrahigh intrinsic Q factor of $Q_i \approx 3.4 \times 10^6$. From the measured spectra, we observe a maximum loaded Q factor of $Q_{\text{load}} \approx 2.1 \times 10^6$. These results represent the highest Q factor ever demonstrated in an FP cavity on SOI. The high performance is enabled by a novel on-chip retroreflector working in the multimode regime. The reflectivity of the proposed retroreflector is supported by the naturally low-loss and broadband TIR effect. Moreover, the TE_1 mode is employed to dampen the corner scattering and bring the reflection loss to an ultralow level. The experimental results provide strong evidence that this new type of reflector possesses ultralow reflection losses ($RL_{\text{TE}_1} \approx 0.05$ dB) over a broad bandwidth (>100 nm). The performance of several on-chip FP cavities is summarized and compared in Table 1. The reflection loss of the proposed retroreflector is comparable to that of the bulk

DBR with microscale trenches. Compared to the previous results on silicon, the demonstrated Q factor has been improved by more than 2 orders of magnitude. Usually, such high Q factors can only be accomplished by using bulky silica waveguides with an ultralow index contrast ($\approx 1\%$) [51]. The loaded Q factor can be further enhanced by decreasing the coupling ratio of ADCs. In addition, it is possible to improve the intrinsic Q factor through the utilization of more advanced fabrication technologies (e.g., the photonic Damascene process [52]) or material platforms with a lower index contrast (e.g., SNOI) to reduce the sidewall roughness. The reflection loss can be mitigated by using the hard mask in the dry-etching process to improve the perpendicularity of sidewalls [53]. The measured finesse is as high as $F > 100$, which can be improved to $F > 500$ by reducing the propagation loss (e.g., $\alpha < 0.1$ dB/cm) and coupling ratio (e.g., $T_{\text{CRO,TE}_1} < 0.005$).

Our design has the potential to serve as a versatile platform for numerous applications, including, but not limited to, comb lasers and linewidth narrowing. The proposed FP cavity possesses an ultrahigh Q factor and a relatively small free spectral range. These features are desirable for electrically pumped narrow-linewidth dense comb lasers [5]. It is anticipated that a low-threshold low-repetition-rate comb laser could be realized via the heterogeneous integration with thin-filmed III-V gain materials. Another potential application is linewidth narrowing, which is to suppress close-to-carrier noises of lasers by using an ultrahigh- Q cavity isolated in a cryogenic environment [6]. The large modal volume of the proposed FP cavity could help to mitigate optical nonlinearity and optothermal phase noises [40]. Overall, this work demonstrates a novel method for realizing ultralow-loss on-chip reflectors for the use in ultrahigh- Q integrated FP cavities, which enriches the silicon photonic toolbox and paves ways for numerous applications.

APPENDIX A: FABRICATION-TOLERANCE ANALYSIS OF ADCS

The fabricated ADC usually has deviated core dimensions and gap widths as a result of imperfect patterning and etching. In addition, the silicon core thickness is not homogeneous at the wafer scale. Therefore, it is vital to ensure that the designed ADC is immune to these fabrication defects. Figure 6 shows the calculated $T_{\text{CRO,TE}_1}$ and CL with $\delta W_{\text{wg}} = \pm 10$ nm, $\delta W_{\text{gap}} = \pm 10$ nm, and $\delta H_{\text{wg}} = \pm 10$ nm. It can be found that the deviation range of $T_{\text{CRO,TE}_1}$ is quite small. Ultralow coupling losses of $CL < 0.01$ dB can be also maintained.

Table 1. Performance Comparison of On-Chip FP Cavities

Reference	Platform	Reflector Type	RL [dB]	BW [nm]	FSR [nm]	α [dB/cm]	Q_{load}	Q_i	F
[8]	SNOI	DBR	/	≈ 7	1.39	0.33	4.8×10^5	/	430
[10]	SOI	DBR	/	≈ 1	/	10.3	3.4×10^4	/	/
[11]	SOI	Loop	/	> 4	1.3	5–8	2.3×10^4	/	19
[15]	SOI	DBR	0.22	80	31.3	/	1.3×10^3	2.6×10^4	26
[19]	SOI	DBR	0.32	> 80	30	/	1.4×10^4	/	270
[20]	Bulk Si	DBR	0.03	> 200	29.4	1.32	2.7×10^4	/	500
[21]	SOI	Metallic mirror	0.97	200	21	/	3.6×10^2	9.0×10^2	5
[22]	SOI	Inverse design	0.71	200	≈ 10	/	2.0×10^3	4.1×10^3	13
This work	SOI	Retroreflector	0.05	> 100	< 0.16	0.18	2.1×10^6	3.4×10^6	> 100

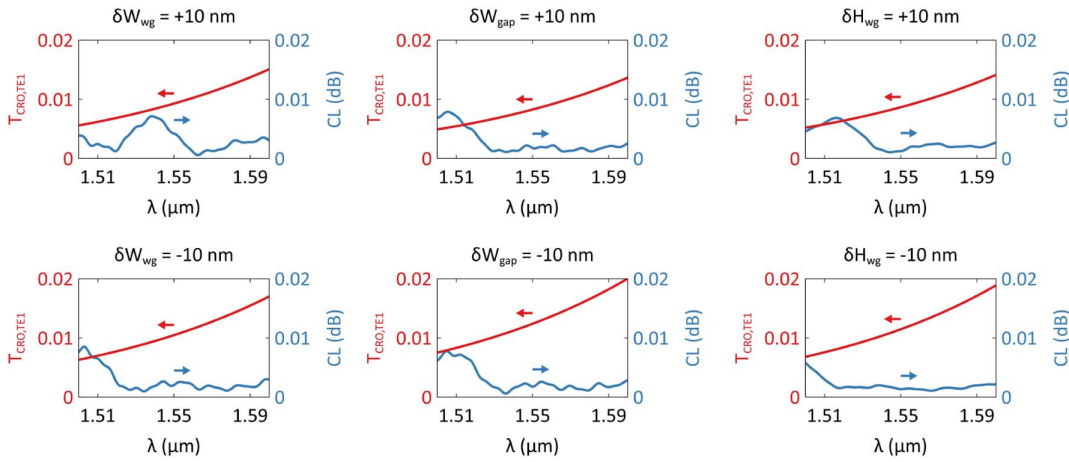


Fig. 6. Calculated TE₁-coupling ratio (T_{CRO,TE_1}) and coupling-loss (CL) spectra with parameter deviations.

APPENDIX B: ADDITIONAL MEASUREMENT RESULTS

Figures 7(a) and 7(b) show the measured T_{FP} spectra at different wavelength bands with $L_{tp} = 1.5$ mm and 4 mm. The

highest loaded Q factor ($Q_{load} \approx 2.1 \times 10^6$) is attained around $\lambda \approx 1.51 \mu\text{m}$. The increasing Q_{load} and decreasing ER_{res} can be observed at shorter wavelengths, which is due to the dispersion of T_{CRO,TE_1} . In Fig. 7(c), the measured extinction ratio ranges

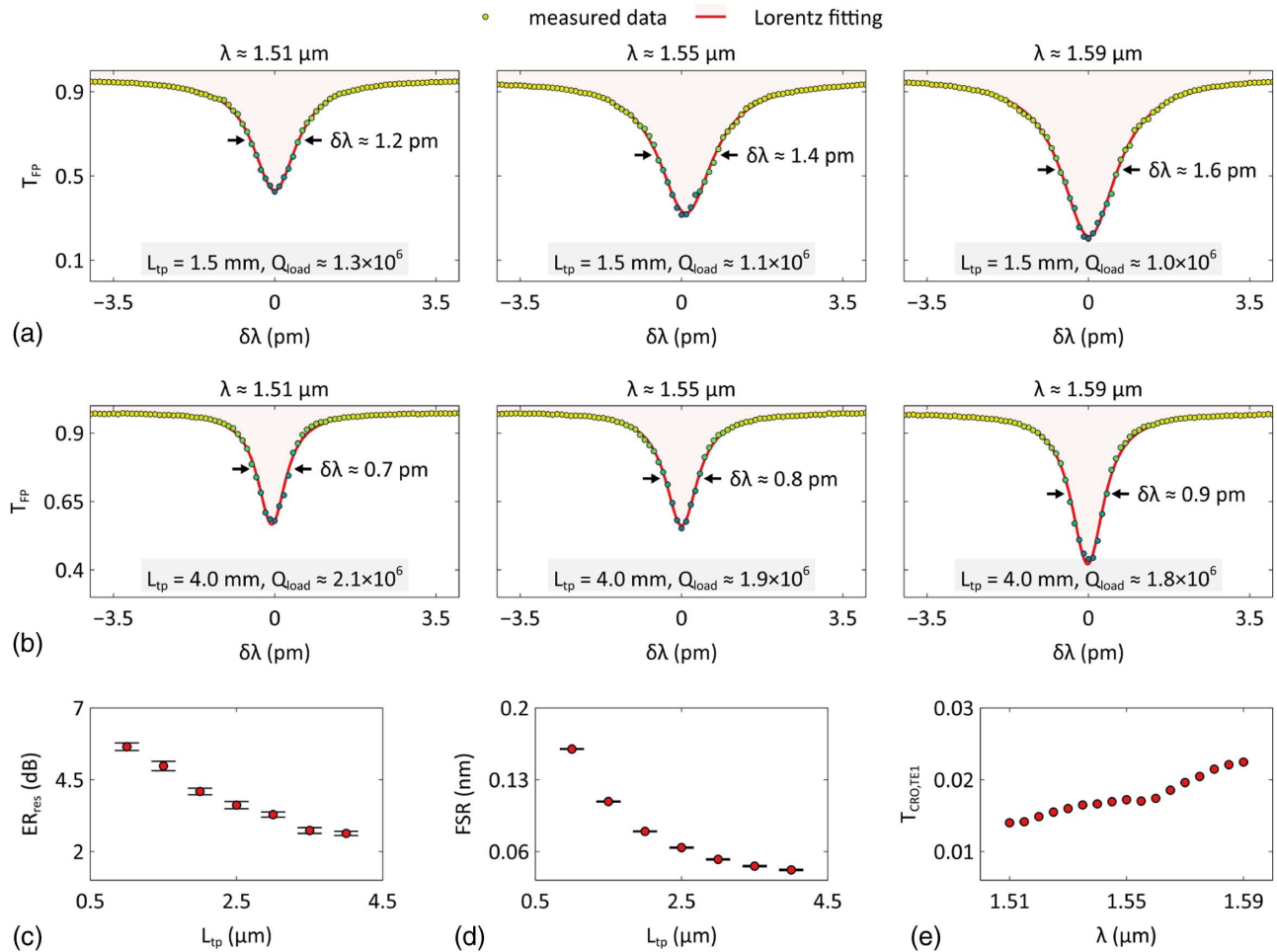


Fig. 7. Measured transmittance (T_{FP}) spectra at different wavelength bands ($\lambda \approx 1.51, 1.55,$ and $1.59 \mu\text{m}$) with taper lengths of (a) $L_{tp} = 1.5$ mm and (b) 4.0 mm; measured (c) extinction ratios (ER_{res}) and (d) free spectral ranges (FSRs) with varying L_{tp} ; (e) reconstructed TE₁ coupling-ratio (T_{CRO,TE_1}) spectrum.

from $ER_{\text{res}} \approx 5.7$ dB to 2.6 dB as the taper length varies from $L_{\text{tp}} = 1.0$ mm to 4.5 mm. Figure 7(d) shows the measured $L_{\text{tp}} - \text{FSR}$ curve. The reconstructed $T_{\text{CRO,TE}_1}$ spectrum is plotted in Fig. 7(e). At the central wavelength, the TE_1 coupling ratio is measured to be $T_{\text{CRO,TE}_1} \approx 0.017$.

Funding. Research Grants Council, University Grants Committee, General Research Fund (14203620).

Acknowledgment. The authors acknowledge Applied Nanotools Inc. for enabling the device fabrication. H. Xu thanks ITF Research Talent Hub for the financial support.

Disclosures. The authors declare no conflicts of interest.

Data Availability. Data underlying the results presented in this paper are not publicly available at this time but may be obtained from the authors upon reasonable request.

REFERENCES

- M. H. Bitarafan and R. G. DeCorby, "On-chip high-finesse Fabry-Perot microcavities for optical sensing and quantum information," *Sensors* **17**, 1748 (2017).
- J. Nicholas Porter, J. S. Jackson, D. S. Durfee, and R. L. Sandberg, "Laser wavelength metrology with low-finesse etalons and Bayer filters," *Opt. Express* **28**, 37788–37797 (2020).
- C. Graf, A. Thuring, H. Vahlbruch, K. Danzmann, and R. Schnabel, "Length sensing and control of a Michelson interferometer with power recycling and twin signal recycling cavities," *Opt. Express* **21**, 5287–5299 (2013).
- A. A. Trichet, J. Foster, N. E. Otori, D. James, P. R. Dolan, G. M. Hughes, C. Vallance, and J. M. Smith, "Open-access optical microcavities for lab-on-a-chip refractive index sensing," *Lab Chip* **14**, 4244–4249 (2014).
- Z. Wang, K. Van Gasse, V. Moskalenko, S. Latkowski, E. Bente, B. Kuyken, and G. Roelkens, "A III-V-on-Si ultra-dense comb laser," *Light Sci. Appl.* **6**, e16260 (2017).
- T. Kessler, C. Hagemann, C. Grebing, T. Legero, U. Sterr, F. Riehle, M. J. Martin, L. Chen, and J. Ye, "A sub-40-mHz-linewidth laser based on a silicon single-crystal optical cavity," *Nat. Photonics* **6**, 687–692 (2012).
- G. Cui, J. M. Hannigan, R. Loeckenhoff, F. M. Matinaga, M. G. Raymer, S. Bhongale, M. Holland, S. Mosor, S. Chatterjee, H. M. Gibbs, and G. Khitrova, "A hemispherical, high-solid-angle optical micro-cavity for cavity-QED studies," *Opt. Express* **14**, 2289–2299 (2006).
- S. Xie, Y. Zhang, Y. Hu, S. Villeux, and M. Dagenais, "On-chip Fabry-Perot Bragg grating cavity enhanced four-wave mixing," *ACS Photon.* **7**, 1009–1015 (2020).
- S.-P. Yu, H. Jung, T. C. Briles, K. Srinivasan, and S. B. Papp, "Photonic-crystal-reflector nanoresonators for Kerr-frequency combs," *ACS Photon.* **6**, 2083–2089 (2019).
- W. Zhang, N. Ehteshami, W. Liu, and J. Yao, "Silicon-based on-chip electrically tunable sidewall Bragg grating Fabry-Perot filter," *Opt. Lett.* **40**, 3153–3156 (2015).
- R. Ge, Y. Luo, S. Gao, Y. Han, L. Chen, and X. Cai, "Reconfigurable silicon bandpass filters based on cascaded Sagnac loop mirrors," *Opt. Lett.* **46**, 580–583 (2021).
- C. Renaut, J. Dellinger, B. Cluzel, T. Honegger, D. Peyrade, E. Picard, F. De Fornel, and E. Hadji, "Assembly of microparticles by optical trapping with a photonic crystal nanocavity," *Appl. Phys. Lett.* **100**, 101103 (2012).
- A. Reiserer, C. Nölleke, S. Ritter, and G. Rempe, "Ground-state cooling of a single atom at the center of an optical cavity," *Phys. Rev. Lett.* **110**, 223003 (2013).
- W. Bogaerts and L. Chrostowski, "Silicon photonics circuit design: methods, tools and challenges," *Laser Photon. Rev.* **12**, 1700237 (2018).
- Q. Huang, Q. Liu, and J. Xia, "Traveling wave-like Fabry-Perot resonator-based add-drop filters," *Opt. Lett.* **42**, 5158–5161 (2017).
- H. C. Kim, K. Ikeda, and Y. Fainman, "Resonant waveguide device with vertical gratings," *Opt. Lett.* **32**, 539–541 (2007).
- H.-C. Kim, K. Ikeda, and Y. Fainman, "Tunable transmission resonant filter and modulator with vertical gratings," *J. Lightwave Technol.* **25**, 1147–1151 (2007).
- M. G. Saber, Y. Wang, E. El-Fiky, D. Patel, K. A. Shahriar, M. S. Alam, M. Jacques, Z. Xing, L. Xu, N. Abadia, and D. V. Plant, "Transversely coupled Fabry-Perot resonators with Bragg grating reflectors," *Opt. Lett.* **43**, 13–16 (2018).
- Y. Wang, S. Gao, K. Wang, H. Li, and E. Skafidas, "Ultra-broadband, compact, and high-reflectivity circular Bragg grating mirror based on 220 nm silicon-on-insulator platform," *Opt. Express* **25**, 6653–6663 (2017).
- M. W. Pruessner, T. H. Stievater, and W. S. Rabinovich, "Integrated waveguide Fabry-Perot microcavities with silicon/air Bragg mirrors," *Opt. Lett.* **32**, 533–535 (2007).
- S. Zamek, L. Feng, M. Khajavikhan, D. T. Tan, M. Ayache, and Y. Fainman, "Micro-resonator with metallic mirrors coupled to a bus waveguide," *Opt. Express* **19**, 2417–2425 (2011).
- Z. J. Yu, H. R. Cui, and X. K. Sun, "Genetically optimized on-chip wideband ultracompact reflectors and Fabry-Perot cavities," *Photon. Res.* **5**, B15–B19 (2017).
- Y. Takahashi, Y. Inui, M. Chihara, T. Asano, R. Terawaki, and S. Noda, "A micrometre-scale Raman silicon laser with a microwatt threshold," *Nature* **498**, 470–474 (2013).
- S. Jeon, B. S. Song, S. Yamada, Y. Yamaguchi, J. Upham, T. Asano, and S. Noda, "Multiple-channel wavelength conversions in a photonic crystal cavity," *Opt. Express* **23**, 4523–4528 (2015).
- A. D. Osterkryger, J. R. de Lasson, M. Heuck, Y. Yu, J. Mork, and N. Gregersen, "Spectral symmetry of Fano resonances in a waveguide coupled to a microcavity," *Opt. Lett.* **41**, 2065–2068 (2016).
- X. C. Ji, J. K. Jang, U. D. Dave, M. Corato-Zanarella, C. Joshi, A. L. Gaeta, and M. Lipson, "Exploiting ultralow loss multimode waveguides for broadband frequency combs," *Laser Photon. Rev.* **15**, 2000353 (2021).
- L. Zhang, L. L. Jie, M. Zhang, Y. Wang, Y. W. Xie, Y. C. Shi, and D. X. Dai, "Ultrahigh-Q silicon racetrack resonators," *Photon. Res.* **8**, 684–689 (2020).
- M. Soltani, S. Yegnanarayanan, and A. Adibi, "Ultra-high Q planar silicon microdisk resonators for chip-scale silicon photonics," *Opt. Express* **15**, 4694–4704 (2007).
- S. Liu, W. Z. Sun, Y. J. Wang, X. Y. Yu, K. Xu, Y. Z. Huang, S. M. Xiao, and Q. H. Song, "End-fire injection of light into high-Q silicon microdisks," *Optica* **5**, 612–616 (2018).
- S. Gao, Y. Wang, K. Wang, and E. Skafidas, "High contrast circular grating reflector on silicon-on-insulator platform," *Opt. Lett.* **41**, 520–523 (2016).
- H. Xu and Y. Shi, "Silicon-waveguide-integrated high-quality meta-grating supporting bound state in the continuum," *Laser Photon. Rev.* **14**, 1900430 (2020).
- Y. Wang, S. Gao, K. Wang, and E. Skafidas, "Ultra-broadband and low-loss 3 dB optical power splitter based on adiabatic tapered silicon waveguides," *Opt. Lett.* **41**, 2053–2056 (2016).
- D. J. Thomson, Y. Hu, G. T. Reed, and J.-M. Fedeli, "Low loss MMI couplers for high performance MZI modulators," *IEEE Photon. Technol. Lett.* **22**, 1485–1487 (2010).
- H. Xu and Y. Shi, "Flat-top CWDM (de)multiplexer based on MZI with bent directional couplers," *IEEE Photon. Technol. Lett.* **30**, 169–172 (2018).
- H. Xu, D. Dai, and Y. Shi, "Ultra-broadband on-chip multimode power splitter with an arbitrary splitting ratio," *OSA Contin.* **3**, 1212–1221 (2020).
- Y. Wang and D. Dai, "Multimode silicon photonic waveguide corner-bend," *Opt. Express* **28**, 9062–9071 (2020).

37. M. Born, E. Wolf, and A. B. Bhatia, *Principles of Optics: Electromagnetic Theory of Propagation, Interference, and Diffraction of Light* (Cambridge University, 2019).
38. R. C. Weast, *CRC Handbook of Chemistry and Physics* (CRC Press, 1988).
39. Lumerical Inc., <https://www.lumerical.com/>.
40. M. W. Puckett, K. Liu, N. Chauhan, Q. Zhao, N. Jin, H. Cheng, J. Wu, R. O. Behunin, P. T. Rakich, K. D. Nelson, and D. J. Blumenthal, "422 Million intrinsic quality factor planar integrated all-waveguide resonator with sub-MHz linewidth," *Nat. Commun.* **12**, 934 (2021).
41. H. K. Tsang, M. W. K. Mak, L. Y. Chan, J. B. D. Soole, C. Youtsey, and I. Adesida, "Etched cavity InGaAsP/InP waveguide Fabry-Perot filter tunable by current injection," *J. Lightwave Technol.* **17**, 1890–1895 (1999).
42. D. Dai, J. Wang, and Y. Shi, "Silicon mode (de)multiplexer enabling high capacity photonic networks-on-chip with a single-wavelength-carrier light," *Opt. Lett.* **38**, 1422–1424 (2013).
43. J. F. Bauters, M. J. Heck, D. John, D. Dai, M. C. Tien, J. S. Barton, A. Leinse, R. G. Heideman, D. J. Blumenthal, and J. E. Bowers, "Ultra-low-loss high-aspect-ratio Si₃N₄ waveguides," *Opt. Express* **19**, 3163–3174 (2011).
44. Y. Fu, T. Ye, W. Tang, and T. Chu, "Efficient adiabatic silicon-on-insulator waveguide taper," *Photon. Res.* **2**, A41–A44 (2014).
45. H. F. Taylor and A. Yariv, "Guided wave optics," *Proc. IEEE* **62**, 1044–1060 (1974).
46. Applied Nanotools Inc., <https://www.appliednt.com/>.
47. V. R. Almeida, R. R. Panepucci, and M. Lipson, "Nanotaper for compact mode conversion," *Opt. Lett.* **28**, 1302–1304 (2003).
48. H. Xu, D. Dai, and Y. Shi, "Fabrication-friendly on-chip silicon polarizer based on polarization-selective corner mirrors," *IEEE Photon. Technol. Lett.* **33**, 652–655 (2021).
49. W. Jin, Q.-F. Yang, L. Chang, B. Shen, H. Wang, M. A. Leal, L. Wu, M. Gao, A. Feshali, M. Paniccia, K. J. Vahala, and J. E. Bowers, "Hertz-linewidth semiconductor lasers using CMOS-ready ultra-high-Q microresonators," *Nat. Photonics* **15**, 346–353 (2021).
50. L. Zhang, S. A. Hong, Y. Wang, H. Yan, Y. W. Xie, T. N. Chen, M. Zhang, Z. J. Yu, Y. C. Shi, L. Liu, and D. X. Dai, "Ultralow-loss silicon photonics beyond the singlemode regime," *Laser Photon. Rev.* **16**, 2100292 (2022).
51. C. M. Greiner, D. Iazikov, and T. W. Mossberg, "Million-Q reflection-based integrated resonators patterned with deep ultraviolet photolithography," *IEEE Photon. Technol. Lett.* **18**, 2677–2679 (2006).
52. M. H. P. Pfeiffer, A. Kordts, V. Brasch, M. Zervas, M. Geiselmann, J. D. Jost, and T. J. Kippenberg, "Photonic Damascene process for integrated high-Q microresonator based nonlinear photonics," *Optica* **3**, 20–25 (2016).
53. D. H. Lee, S. J. Choo, U. Jung, K. W. Lee, K. W. Kim, and J. H. Park, "Low-loss silicon waveguides with sidewall roughness reduction using a SiO₂ hard mask and fluorine-based dry etching," *J. Micromech. Microeng.* **25**, 015003 (2015).